

***Ab initio* investigation of single-layer high thermal conductivity boron compounds**Hang Fan,^{1,2,3} Huan Wu,¹ Lucas Lindsay,^{4,*} and Yongjie Hu^{1,†}¹*Department of Mechanical and Aerospace Engineering, University of California, Los Angeles, Los Angeles, California 90095, USA*²*School of Mechatronical Engineering, Beijing Institute of Technology, Beijing 100083, China*³*Institute of Chemical Materials, China Academy of Engineering Physics, Mianyang 621900, China*⁴*Materials Science and Technology Division, Oak Ridge National Laboratory, Oak Ridge, Tennessee 37831, USA*

(Received 14 May 2019; revised manuscript received 13 July 2019; published 14 August 2019)

The discovery and design of materials with large thermal conductivities (κ_L) is critical to address future heat management challenges, particularly as devices shrink to the nanoscale. This requires developing novel physical insights into the microscopic interactions and behaviors of lattice vibrations. Here, we use *ab initio* phonon Boltzmann transport calculations to derive fundamental understanding of lattice thermal transport in two-dimensional (2D) monolayer hexagonal boron-based compounds, h-BX ($X = N, P, As, Sb$). Monolayer h-BAs, in particular, possesses structural and dispersion features similar to bulk cubic BAs and 2D graphene, which govern their ultrahigh room temperature κ_L (1300 W/m K and 2000–4000 W/m K, respectively), yet here combine to give significantly lower κ_L for monolayer h-BAs (400 W/m K at room temperature). This work explores this discrepancy, and thermal transport in the monolayer h-BX systems in general, via comparison of the microscopic mechanisms that govern phonon transport. In particular, we present calculations of phonon dispersions, velocities, scattering phase space and rates, and κ_L of h-BX monolayers as a function of temperature, size, defects, and other fundamental parameters. From these calculations, we make predictions of the thermal conductivities of h-BX monolayers, and more generally develop deeper fundamental understanding of phonon thermal transport in 2D and bulk materials.

DOI: 10.1103/PhysRevB.100.085420

I. INTRODUCTION

As microelectronic devices shrink and power densities grow, heat dissipation has become a formidable technology challenge. The discovery of high thermal conductivity materials to improve thermal management and energy efficiency is essential for further gains in device performance. *Ab initio* theoretical tools such as those based on density functional theory (DFT) have been recently developed and demonstrated their capability to precisely calculate thermal properties of materials [1–3]. In particular, boron compounds, including cubic boron phosphide (c-BP) and boron arsenide (c-BAs), were predicted to have high thermal conductivities [4,5]. Importantly, experimental work has demonstrated the synthesis of high-quality crystals and measured thermal conductivity values of 500 and 1300 W/m K, respectively, in c-BP [6] and c-BAs [7–9]. These studies exemplify the power of combined synthesis, characterization, and *ab initio* theory for developing design rules for new materials discovery.

Motivated by these studies, here we perform *ab initio* calculations to examine the thermal properties of two-dimensional (2D) honeycomb structures of these boron compounds [inset, Fig. 1(a)]. We present calculations of the lattice thermal conductivity (κ_L) and spectral phonon transport properties for monolayer hexagonal compounds: h-BN, h-BP, h-BAs, and h-BSb—referred to collectively as h-BX

monolayers. Physical insights relating symmetry, structure, and the vibrational characteristics that build microscopic, mode-specific phonon properties and transport behaviors are developed as the monolayer structures are compared with their bulk counterparts, and criteria for high thermal conductivity are discussed in detail.

II. THEORY AND COMPUTATIONAL DETAILS

In this section, we discuss the underlying theoretical and numerical details used to perform the *ab initio* calculations of thermal transport in the h-BX systems. Further details can be found in the literature [10–12].

A. Boltzmann transport and lattice thermal conductivity

Thermal energy in semiconductor materials is primarily carried by lattice vibrations (quantized modes called phonons), as electrons and other heat carriers (e.g., magnons) usually give negligible contributions. The lattice thermal conductivity here is calculated using an *ab initio* methodology based on DFT and solution of the phonon Boltzmann transport equation (BTE) [13,14], without relying on empirical adjustable parameters. This microscopic transport description explicitly considers mode-dependent quantum phonon-scattering processes and their entangled distribution functions as the Boltzmann equation is solved self-consistently. In particular, a small applied temperature gradient ∇T perturbs the phonon distributions from equilibrium, resulting in a drifting

*lindsayr@ornl.gov

†yhu@seas.ucla.edu

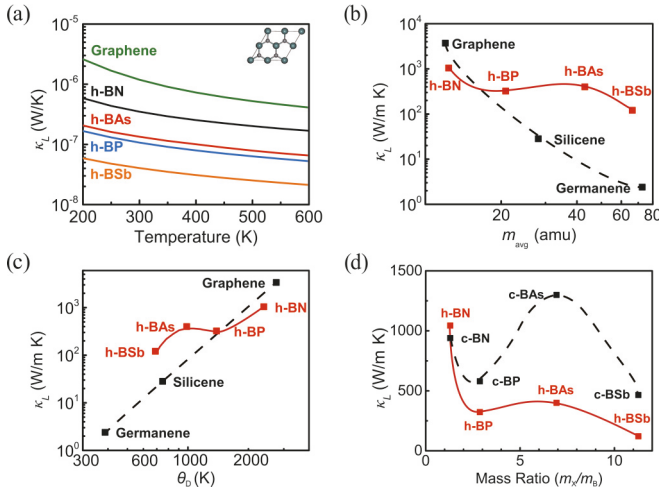


FIG. 1. *Ab initio* calculated thermal conductivity vs temperature and classical metrics. (a) Calculated lattice thermal conductivity κ_L in 2D units as a function of temperature for monolayer graphene (green), h-BN (black), h-BP (blue), h-BAs (red), and h-BSb (orange) with natural isotopic abundances. (Inset) Top view of the hexagonal structure of a diatomic 2D honeycomb crystal. Room temperature κ_L of different materials with natural isotopic abundances vs (b) average atomic mass (m_{avg}), (c) Debye temperature (θ_D), and (d) mass ratio (m_X/m_B): monolayer h-BX (red), elemental monolayer materials (black), and separately bulk cubic-BX (black). Curves in (b)–(d) are guide lines to illustrate the dependence trend.

phonon flux which is balanced by phonon scatterings,

$$\mathbf{v}_\lambda \cdot \nabla T \frac{\partial n_\lambda}{\partial T} = \left(\frac{\partial n_\lambda}{\partial t} \right)_{\text{scattering}}. \quad (1)$$

Here, n_λ is the nonequilibrium distribution function for phonon mode $\lambda \equiv (\mathbf{q}, p)$ with wave vector \mathbf{q} and polarization p , and \mathbf{v}_λ is the phonon group velocity. The right-hand side of Eq. (1) represents the sum of all scatterings that alter n_λ , which are predominantly built from three-phonon interactions determined within quantum perturbation theory [15,16]. Isotopes, boundaries, and other extrinsic phonon-scattering mechanisms are considered in some cases, as discussed below. Phonon frequencies and eigenvectors are determined by diagonalizing the dynamical matrix for each wave vector considered (see Sec. II B). For cases where ∇T does not drive the phonon populations far from equilibrium, the single-mode relaxation time approximation (RTA), where individual scattering rates are calculated with the background phonons in equilibrium, gives a reasonably accurate solution to the BTE [17]. However, if the distributions are driven far from equilibrium, a higher-order correction linear in the temperature gradient, $n_\lambda = n_\lambda^0 + (-\partial n_\lambda^0 / \partial T) \mathbf{F}_\lambda \cdot \nabla T$ should be considered, where n_λ^0 is the Bose-Einstein distribution function, and \mathbf{F}_λ gives a measure of the deviation from equilibrium. In the latter case, the phonon BTE is solved through self-consistent iteration [18,19] to determine \mathbf{F}_λ . The lattice thermal conductivity tensor $\kappa^{\alpha\beta}$ is given by [18]

$$\kappa^{\alpha\beta} = \frac{1}{k_B T^2 \Omega N} \sum_\lambda n_\lambda^0 (n_\lambda^0 + 1) (\hbar \omega_\lambda)^2 v_\lambda^\alpha F_\lambda^\beta, \quad (2)$$

where \hbar , Ω , N , and ω_λ are the reduced Plank constant, the volume of unit cell, the number of \mathbf{q} -mesh points in the first Brillouin zone, and the mode frequency, respectively. α and β are Cartesian directions.

B. Interatomic force constants

The only inputs to this BTE formalism are the harmonic and third-order anharmonic interatomic force constants (IFCs), which determine the phonon dispersions and scatterings, respectively. Fundamentally, the lattice vibrations are determined by the atomic masses and the interatomic potential (U) of the crystal; IFCs are expansion coefficients of U with respect to small atomic displacements from equilibrium,

$$U = U_0 + \frac{1}{2} \sum_{\{l,b,\mu\}} \Phi_{\mu_1\mu_2}(l_1 b_1; l_2 b_2) u_{\mu_1}(l_1 b_1) u_{\mu_2}(l_2 b_2) + \frac{1}{3!} \sum_{\{l,b,\mu\}} \Phi_{\mu_1\mu_2\mu_3}(l_1 b_1; l_2 b_2; l_3 b_3) u_{\mu_1}(l_1 b_1) u_{\mu_2}(l_2 b_2) u_{\mu_3}(l_3 b_3) + \dots \quad (3)$$

where U_0 is the equilibrium potential and Σ is the summation over all numbered indices. $u_\mu(lb)$ denotes the atomic displacement of the b th atom in the l th unit cell from its equilibrium position along the μ ($= x, y, z$) direction. $\Phi_{\mu_1\mu_2}(l_1 b_1; l_2 b_2)$ and $\Phi_{\mu_1\mu_2\mu_3}(l_1 b_1; l_2 b_2; l_3 b_3)$ are second and third-order IFCs, respectively. The first-order derivatives are zero as they are calculated at equilibrium. We calculated all IFCs through the finite-displacement method (numerical derivatives from perturbed supercells) [20–22], and enforced physical constraints on these based on crystal symmetries, derivative permutations, translational invariance, and rotational invariance.

For a flat 2D lattice in the xy plane, reflection symmetry across the z axis results in the vanishing of IFCs involving an odd number of z components [12,23]. Hence, all IFCs like $\Phi_{xz}(l_1 b_1; l_2 b_2)$ are zero, which completely decouples the out-of-plane and in-plane vibrations at the harmonic level. The same is true for third-order IFCs, only those with even numbers of z components are not zero. Physically, this means, e.g., two out-of-plane flexural vibrational modes cannot merge into another out-of-plane vibrational mode. This limits intrinsic phonon-phonon scatterings, and its consequences on thermal transport in h-BX systems will be discussed in Sec. III C. Besides crystal symmetry, IFCs are also constrained by translational invariance [24], rotational invariance [25–27], Born-Huang equilibrium invariance [28] constraints (see Sec. III A), and derivative permutation symmetries. We enforced translational invariance on the third-order IFCs and all constraints on the harmonic IFCs of each 2D material. This results in the correct physical low-frequency dispersion [29]: two linear acoustic branches [one longitudinal (LA), one transverse (TA)] and one quadratic flexural acoustic branch (ZA). Without such an enforcement, numerical issues, such as finite supercell size and small symmetry violations, can give unphysical linear ZA dispersion [30] or imaginary frequencies near the Brillouin-zone center. This quadratic behavior not only varies the phonon velocities, but also the low-frequency scattering rates and thus phonon lifetimes. Precise representation of these low-frequency modes is essential for

an accurate calculation of the thermal conductivity of 2D materials.

C. Phonon scatterings

In this paper, we consider thermal resistance from intrinsic anharmonic three-phonon interactions, point-defect scattering, and boundary scattering. For high-quality single crystals around room temperature (RT), the intrinsic anharmonic scattering dominates thermal transport, which is determined from scattering processes constrained by transition selection rules for energy conservation $\omega_\lambda \pm \omega_{\lambda_1} - \omega_{\lambda_2} = 0$ and momentum conservation $\mathbf{q} \pm \mathbf{q}_1 - \mathbf{q}_2 = \mathbf{G}$. For a normal (N) process, $\mathbf{G} = \mathbf{0}$; while for an umklapp (U) process, $\mathbf{G} \neq \mathbf{0}$, where \mathbf{G} is a reciprocal lattice vector. For real materials, extrinsic resistance arises due to phonon interactions with lattice imperfections. Here we considered phonon-point-defect interactions (isotopes and vacancies) due to mass perturbations [31,32]. Defect-induced force constant perturbations and structural relaxation have been shown to be important for vacancies, but give the same general trends as the mass perturbation scattering in reducing thermal conductivity, although for significantly lower defect concentrations [33,34]. Boundary scattering is caused by limited sample size, which becomes especially important at low temperature or in nanostructures where phonon mean-free paths are relatively long compared to the sample size. Here we calculated phonon mean-free path spectra for the h-BX monolayers and evaluated width-dependent κ_L with an empirical boundary scattering model (see Sec. III E).

Within the RTA these separate phonon-scattering mechanisms can be linearly combined via Matthiessen's rule to determine phonon lifetimes as

$$\frac{1}{\tau_\lambda} = \left(\frac{1}{\tau_\lambda} \right)_{\text{anharmonic}} + \left(\frac{1}{\tau_\lambda} \right)_{\text{defect}} + \left(\frac{1}{\tau_\lambda} \right)_{\text{boundary}}. \quad (4)$$

Full solution of the BTE in Eq. (1), however, captures the network of interactions that tie the distributions of all the phonons together and is required to more accurately determine phonon transport. In particular, the RTA treats N scattering as purely resistive and therefore underestimates κ_L as U scattering actually degrades the collective phonon flow. Thus, in materials with strong N scattering relative to U scattering the κ_L determined by these two methods can differ substantially. We compare both methods in this work and demonstrate the failure of the RTA (see Sec. III B) in describing κ_L of the h-BX monolayers.

D. DFT details

We used DFT to determine the IFCs, which are the only inputs to the BTE formalism to calculate κ_L , thus no adjustable parameters are used. DFT calculations were performed using the QUANTUM ESPRESSO package [35,36] with norm-conserving pseudopotentials in the local-density approximation (LDA) [37,38]. For h-BX, we first optimized the structure using a $31 \times 31 \times 1q$ mesh and a convergence precision for energies and forces taken as 10^{-10} Ry and 10^{-6} Ry/bohr, respectively. The kinetic energy cutoff for all calculations was 80 Ry. All IFCs were calculated using atomic

perturbations of supercells with 128 atoms and 15-Å vacuum distance between periodic layer images. The harmonic IFCs determine the phonon frequencies, eigenvectors, and velocities (see Sec. III A). The anharmonic IFCs determine the phonon-phonon coupling matrix elements (see Sec. III B). The lattice thermal conductivity is built from transport lifetimes determined from full solution of the linearized BTE using the shengBTE code [18]. For graphene, we used the IFCs from the almbabte [39] database. For 2D materials, the definition of thickness is fairly arbitrary. In Fig. 1(a), we use 2D units of thermal conductivity (W/K), which are independent of the arbitrarily defined monolayer thickness. In the rest of the paper, the thickness 3.35 Å (typical value chosen for the thickness of graphene) is used in the thermal conductivity calculations for comparison with bulk values and physical intuition. Note that this thickness simply scales the thermal conductivity, which can be easily changed to compare with other definitions of the monolayer thickness. For c-BAs, we used the same DFT settings as Ref. [7]. For c-BP, we used the LDA projector-augmented wave pseudopotential [40]. The electronic structure calculations were done with 80-Ry plane-wave cutoff kinetic energy and $6 \times 6 \times 6 k$ meshes. The second-order IFCs were calculated by density-functional perturbation theory [41] with a k -point mesh of $6 \times 6 \times 6$ using the QUANTUM ESPRESSO package [35,36]. The third-order IFCs were calculated by the finite-displacement method on 128-atom supercells and cut off at eighth-nearest-neighboring atoms. The convergence test of thermal conductivity versus supercell size, mesh size, cutoff radius for third-order IFCs, and scalebroad settings are included in Appendix A.

III. RESULTS AND DISCUSSION

Calculated lattice thermal conductivities for monolayer h-BX compounds are given in Fig. 1. The 2D h-BX compounds have higher κ_L than most other 2D group-IV and III-V compounds reported in the literature [42–45], which typically have buckled structures. After full structural relaxation, each h-BX system remained flat [inset, Fig. 1(a)], i.e., buckling of these monolayers was not energetically favorable as was found for graphene's elemental cousins, silicene and germanene [44]. The calculated RT κ_L of h-BX monolayers with natural isotopic abundances are 1045, 323, 399, and 121 W/m K, respectively, for h-BN, h-BP, h-BAs, and h-BSb using thickness of 3.35 Å. The isotopically pure κ_L at RT are 1242, 374, 457, and 160 W/m K for h-BN, h-BP, h-BAs, and h-BSb, respectively. From 200 to 600 K, κ_L decreases monotonically for each system due to enhanced intrinsic anharmonic scattering from thermal population of higher-frequency phonons.

We evaluate κ_L of h-BX monolayers with conventional criteria used to understand thermal conductivity, rules of thumb proposed by Slack [46]. High lattice thermal conductivity generally occurs in materials with simple structure, small average atomic mass (m_{avg}), large Debye temperature (θ_D), and low anharmonicity. Insights from first-principles calculations of κ_L of bulk GaN [47], BAs [4,48], and Li₂Se [49] demonstrated that these rules should be augmented to consider the mass difference between constituent atoms in compound

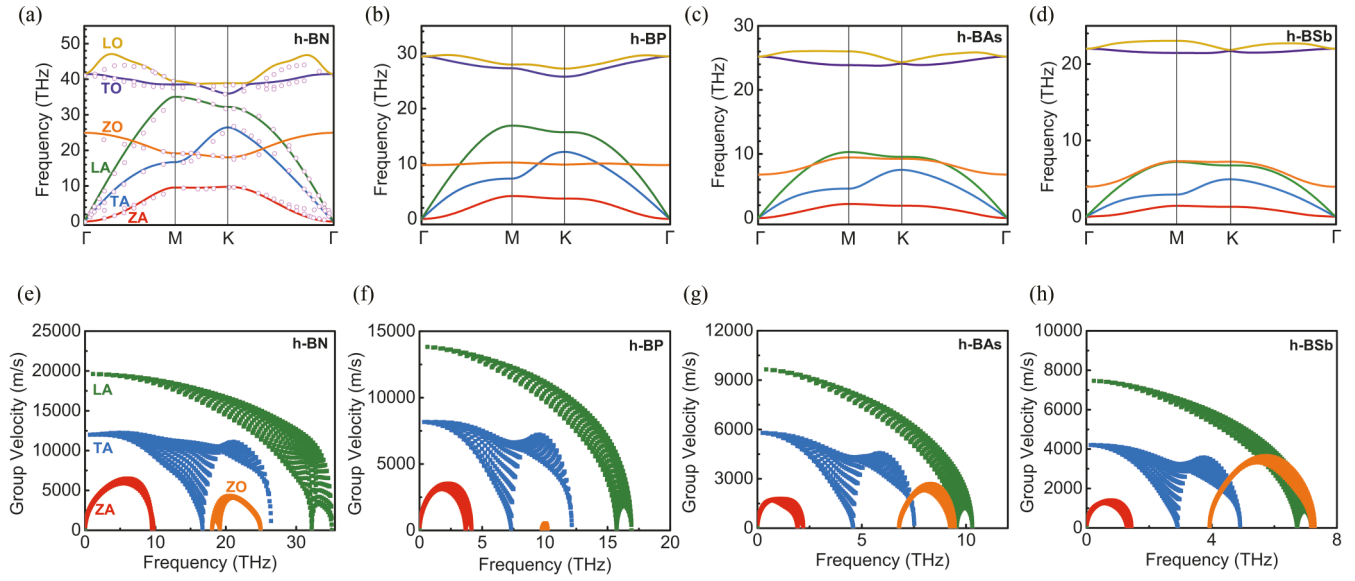


FIG. 2. Calculated phonon dispersions and mode-dependent group velocities. Calculated phonon dispersions in high-symmetry directions for hexagonal monolayer (a) h-BN, (b) h-BP, (c) h-BAs, and (d) h-BSb. Circle symbols in (a) correspond to experimental data for bulk h-BN determined by inelastic x-ray scattering [54]. (e)–(h) For the same systems, calculated lower-frequency phonon group velocities vs phonon frequencies of different polarizations: ZA (red), TA (blue), LA (green), and ZO (orange).

materials and how closely the acoustic branches, and separately the optic branches, are packed together. The former determines the frequency gap between acoustic phonons and high-frequency optic modes, which governs the number of acoustic-acoustic-optic scattering channels for the heat-carrying acoustic phonons via energy conservation. The latter determines how many all-acoustic and acoustic-optic interactions are possible. Thus, in materials with a large acoustic-optic frequency gap, closely packed acoustic branches, and small optic bandwidth, scattering resistance is limited and κ_L can be large [4,48].

Figure 1 gives κ_L of h-BX monolayers as a function of (b) m_{avg} , (c) θ_D , and (d) mass ratio, in comparison with their bulk cubic counterparts [48] and elemental monolayers [44]—graphene, silicene, and germanene. As shown in Figs. 1(b) and 1(c), κ_L of graphene, silicene, and germanene all decrease monotonically with increasing m_{avg} and decreasing θ_D , following the conventional criteria and similar to the behavior of their bulk cubic counterparts—diamond, silicon, and germanium [4,48]. However, κ_L values for bulk [4,7,48] and monolayer BAs deviate from these trends. This deviation and unusually high thermal conductivity of c-BAs is understood in terms of the large mass ratio between boron and arsenic atoms and tightly packed acoustic branches [4,48]. Despite monolayer h-BAs and bulk c-BAs demonstrating similar trends, h-BAs does not realize an ultrahigh κ_L as naively expected, particularly when considering its similarities to graphene which also has unusually high κ_L (h-BAs: 399 W/m K; c-BAs: 1300 W/m K [7]; graphene: 2000–4000 W/m K [11,50–52]). *What is the microscopic basis for the extra thermal resistance in h-BAs compared with c-BAs and graphene?* In the following sections, we develop physical insights into the phonon transport behaviors of h-BAs and the other h-BX monolayers by comparing their fundamental

vibrational properties with those of their bulk counterparts, and the elemental monolayers, including phonon dispersions, scattering phase spaces [53], and scattering rates.

A. Phonon band structures and scattering phase space

The phonon dispersion of each 2D h-BX material consists of six branches [Figs. 2(a)–2(d)]: two flexural out-of-plane vibrations (one acoustic ZA and one optic ZO) and four in-plane branches [longitudinal acoustic (LA), longitudinal optic (LO), transverse acoustic (TA), and transverse optic (TO)]. The calculated phonon dispersion of monolayer h-BN is compared with the measured dispersion of bulk h-BN by inelastic X-ray scattering [54]. Note that near the Γ point, the dispersion of the TA and LA branches are linear, while the ZA branch is quadratic. Similar quadratic behavior has been shown for the dispersion of flexural acoustic waves in thin membranes by continuum elastic mechanics [55]. This quadratic flexure behavior is a characteristic of lower dimensional materials (e.g., nanotubes [56,57], graphene [58], borophene [29]), and necessary for accurate calculation of their equilibrium κ_L values. Often in calculations, numerical issues such as residual strain, finite supercell size, and small symmetry violations can lead to unphysical linear dispersion or imaginary frequencies of the ZA branch near the zone center. The quadratic behavior of the ZA branch [Figs. 2(a)–2(d)] is guaranteed by enforcing rotational invariance [25–27].

$$\begin{aligned} & \sum_{l_2 b_2} \Phi_{\mu_1 \mu_2}(0b_1; l_2 b_2) [x_{\mu_3}(l_2 b_2) - x_{\mu_3}(0b_1)] \\ &= \sum_{l_2 b_2} \Phi_{\mu_1 \mu_3}(0b_1; l_2 b_2) [x_{\mu_2}(l_2 b_2) - x_{\mu_2}(0b_1)] \end{aligned} \quad (5)$$

and Born-Huang equilibrium conditions [28]

$$[\mu_1\mu_2; \mu_3\mu_4] = [\mu_3\mu_4; \mu_1\mu_2], \quad (6)$$

with

$$[\mu_1\mu_2; \mu_3\mu_4] = - \sum_{b_1 b_2} \sum_{l_2} \Phi_{\mu_1\mu_2}(0b_1; l_2 b_2) [x_{\mu_3}(l_2 b_2) - x_{\mu_3}(0b_1)] [x_{\mu_4}(l_2 b_2) - x_{\mu_4}(0b_1)] \quad (7)$$

by nominally altering the “as-calculated” DFT harmonic IFCs using a χ^2 minimization procedure [24,59]. Here, $x_\mu(lb)$ is the μ th Cartesian position of the b th atom in the l th unit cell. The quadratic nature of the ZA branch in each h-BX material is most clearly demonstrated by the group velocities approaching zero near the Brillouin-zone center [Figs. 2(e)–2(h)].

The group velocities of the heat carriers play a critical role in determining material thermal conductivity. The group velocities of the h-BX monolayers [Figs. 2(e)–2(h)] generally decrease with increasing average mass in going from h-BN to h-BSb. This is expected as the acoustic frequencies, and thus low-frequency velocities, generally scale inversely with the square root of the heaviest atomic mass [60]. The non-monotonic behavior of κ_L values of h-BX monolayers with m_{avg} in Fig. 1(b) and for c-BX [48] violates this reasoning, thus demonstrating the critical importance of phonon-scattering resistance in determining κ_L . This will be discussed in detail below.

Comparing phonon band structures of h-BX monolayers [Figs. 2(a)–2(d)], the phonon band gap below the upper optical branches (TO and LO) increases significantly from h-BN (0.88 THz) to h-BSb (14.14 THz) as a result of increasing mass ratio. Unlike bulk c-BX systems, h-BX monolayers have a midfrequency ZO phonon branch near the top of the transverse acoustic spectrum in each material. This does not shift appreciably with increasing mass and mass ratio. This ZO branch may play an important role in scattering of the heat-carrying acoustic modes in h-BX monolayers, and may partly explain the lower κ_L value in h-BAs compared with c-BAs, although it does not explain the discrepancy when compared with graphene which has a similar ZO branch. The effects of ZO phonon scattering and the h-BAs/c-BAs/graphene discrepancies will be discussed in more detail in Secs. III C and III D below.

Two features determine the phonon scattering that limits thermal conductivity: (1) strength of scattering interactions as determined by anharmonicity and (2) amount of scattering channels available as determined by energy and momentum conservation conditions. The latter has been shown to be a strong indicator of calculated κ_L values when comparing over a variety of materials [53,61]. This is quantified for each system considered here by calculating the scattering phase space (P_3) of each phonon mode λ by integrating over energy- and momentum-conserving delta functions [53]

$$P_{3\lambda} = \frac{2}{3m^3} \left(P_{3\lambda}^{(+)} + \frac{1}{2} P_{3\lambda}^{(-)} \right), \quad (8)$$

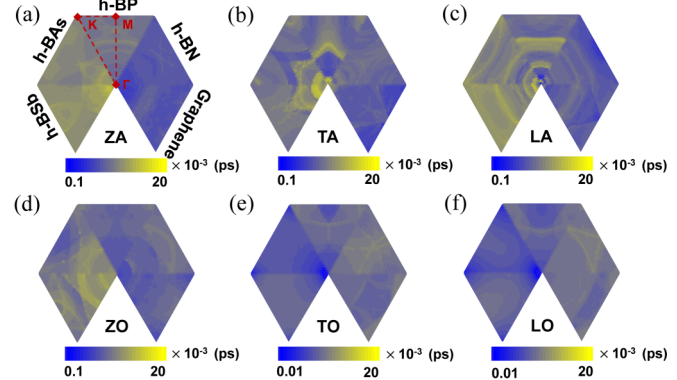


FIG. 3. Phonon scattering phase space. Contour plot of the three-phonon phase space for each phonon branch in h-BX monolayers and graphene: (a) ZA, (b) TA, (c) LA, (d) ZO, (e) TO, and (f) LO, in the irreducible segment of the Brillouin zone.

where

$$P_{3\lambda}^{(\pm)} = \frac{1}{N} \sum_{\lambda', \lambda''} \delta(\omega_\lambda \pm \omega_{\lambda'} - \omega_{\lambda''}) \delta_{\mathbf{q} \pm \mathbf{q}', \mathbf{q}'' + \mathbf{G}}, \quad (9)$$

where m is the number of phonon branches, “ \pm ” corresponds to absorption and emission processes, respectively, and the total scattering phase space is $P_3^{\text{total}} = \frac{1}{N} \sum_{\lambda} P_{3\lambda}$. In addition to energy and momentum conservation, we note that reflection symmetry of the planar 2D materials introduces an additional selection rule (as discussed in Sec. II B) that forbids three-phonon processes involving odd numbers of out-of-plane vibrations and thus further restricts the phonon-scattering phase space [12,23]. This reflection symmetry has been considered in determining the phase-space calculations in this work. The calculated total scattering phase-space values for graphene, h-BN, h-BP, h-BAs, and h-BSb are 0.00327, 0.00396, 0.00484, 0.00584, and 0.00785 ps, respectively. Graphene has the smallest total scattering phase space among the calculated materials, and the total scattering phase space increases monotonically with m_{avg} from h-BN to h-BSb. This is understood in terms of the larger atomic mass scaling down the phonon frequency, and thus increasing the phase space as the energy-conserving delta function in Eq. (9) scales like $\delta(\beta\omega) = \frac{1}{\beta} \delta(\omega)$, where β is a scaling factor of ω [53]. As demonstrated in Fig. 3, for the ZA, TA, LA, and ZO modes, the mode-dependent scattering phase space generally shows the same increasing trend with m_{avg} as that of the total scattering phase space, but the difference of P_3 is weaker for TO and LO modes going from h-BN to h-BSb. The nonmonotonic behavior of κ_L is difficult to understand in terms of the phonon-scattering phase space increasing and the mode velocities decreasing with increasing m_{avg} .

Besides the number of scattering channels, the strength of the scattering processes can be important when comparing scattering rates among different materials. To do this, we estimated the anharmonicity of each material by evaluating the mode-dependent Grüneisen parameters [60]

$$\gamma_\lambda = -\frac{\Omega}{\omega_\lambda} \frac{\partial \omega_\lambda}{\partial \Omega}. \quad (10)$$

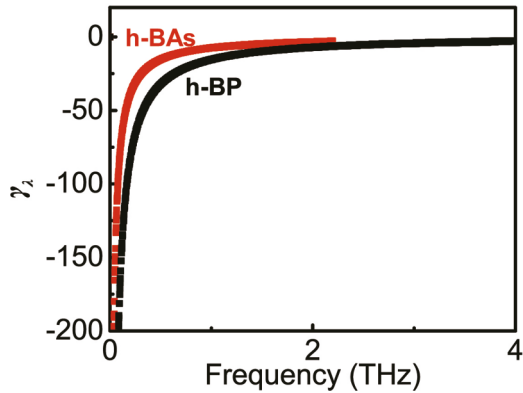


FIG. 4. Mode-dependent Grüneisen parameters (γ_λ) for the ZA branch of h-BAs (red) and h-BP (black) as a function of frequency.

Figure 4 gives the mode-dependent Grüneisen parameters of the ZA branch for h-BP and h-BAs. The γ_λ values for the other branches can be found in Fig. 13. As shown in Fig. 4, h-BAs has smaller magnitude ZA γ_λ than those of h-BP, which indicates the anharmonicity of h-BAs is weaker than h-BP. This also partly explains the higher κ_L of h-BAs compared with that of h-BP. Note that the mode Grüneisen for ZA modes diverge at the Γ point, indicating that a small expansion in the lattice generates a very significant relative increase in phonon frequencies for these modes near the Brillouin-zone center. This is connected with the quadratic behavior becoming linear with lattice strain.

B. Full BTE solution and failure of the RTA

In general, 2D materials are expected to have strong normal scattering relative to umklapp resistance, which leads to the failure of the RTA and gives rise to interesting hydrodynamic transport behaviors [62,63]. In such cases, the full self-consistent solution to the BTE is required to accurately describe thermal transport. Figure 5 gives the ratio of umklapp to normal scattering rates τ_U^{-1}/τ_N^{-1} as a function of phonon frequency for the h-BX monolayers considered here. Normal scattering dominates over umklapp scattering (i.e., $\tau_U^{-1}/\tau_N^{-1} < 1$) for most frequency regimes, particularly for the ZA branches and other low-frequency acoustic modes.

The κ_L for h-BX monolayers from both RTA and full BTE solution calculations are given in Fig. 15, which demonstrates that the RTA fails to accurately describe thermal transport in the h-BX monolayers due to the strong normal scattering. For example, the RT κ_L of h-BN changes from 213 W/m K (RTA value) to 1045 W/m K after iteration. Another interesting point: The thermal conductivity contributions from the different acoustic branches are comparable before iteration as shown in Table I. After iteration, however, the contributions from the ZA branch increases significantly (e.g., for h-BN this increases from 33 to 89%), as the dominance of normal scattering is more significant for the ZA modes compared with the other branches. As shown in Fig. 5, $\tau_N^{-1} > \tau_U^{-1}$ over the whole ZA frequency range, but for LA and TA $\tau_N^{-1} > \tau_U^{-1}$ only for their low-frequency modes. During the iteration, the significant increase in the thermal conductivity contributions

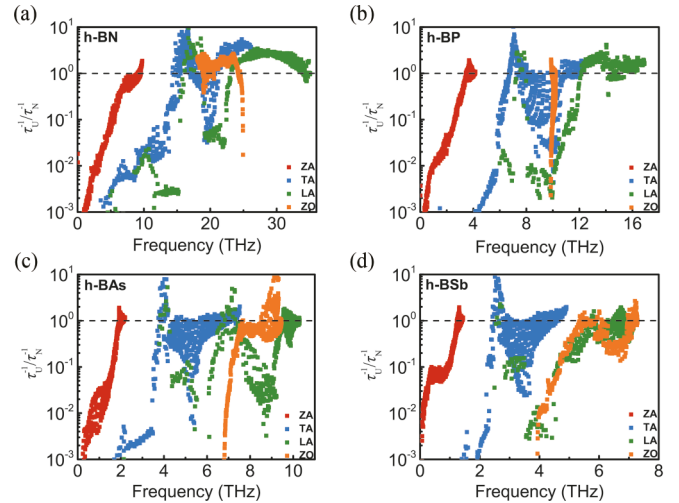


FIG. 5. Comparison of the ratio of umklapp and normal scattering of h-BX monolayers. Calculated ratio of mode-specific scattering rates of umklapp (τ_U^{-1}) and normal (τ_N^{-1}) scattering rates for lower-frequency phonons in (a) h-BN, (b) h-BP, (c) h-BAs, and (d) h-BSb. Colors are used to distinguish different phonon polarizations: ZA (red), TA (blue), LA (green), and ZO (orange).

from the ZA branch implies that the flexural phonons play an important role in single-layer h-BX thermal transport.

C. Comparison of phonon transport between h-BAs and c-BAs

Both c-BAs (RT $\kappa_L = 1300$ W/m K) [7] and h-BAs (RT $\kappa_L = 399$ W/m K) show high κ_L and deviate from the typical trends defined by the conventional criteria for understanding thermal conductivity when compared with the other BX materials. However, κ_L of h-BAs is 70% lower than that of bulk c-BAs despite expectations that this flat monolayer material would conduct heat at least as well given that κ_L of monolayer graphene is larger than that of diamond. High κ_L in c-BAs is attributed to a large phonon band gap and acoustic branch bunching [48]. Figure 6(a) compares the phonon dispersions of h-BAs and c-BAs. Both systems have a large phonon band gap due to the large mass ratio between B and As atoms. For c-BAs, such a large band gap significantly suppresses the acoustic-optic scattering channels. Unlike c-BAs, however, h-BAs has a midfrequency ZO branch near the top of the acoustic frequency spectrum. Thus, in h-BAs energy conservation for acoustic interactions with the ZO branch is easier to

TABLE I. Calculated thermal conductivity contributions from the different acoustic branches.

	Contribution (%)					
	ZA		TA		LA	
	RTA	BTE	RTA	BTE	RTA	BTE
h-BN	32.8	89.1	32.1	6.9	28.6	3.5
h-BP	17.8	68.0	36.5	15.3	18.5	6.2
h-BAs	5.3	43.2	48.8	29.4	42.9	25.8
h-BSb	9.5	37.1	44.3	31.1	44.5	31.7

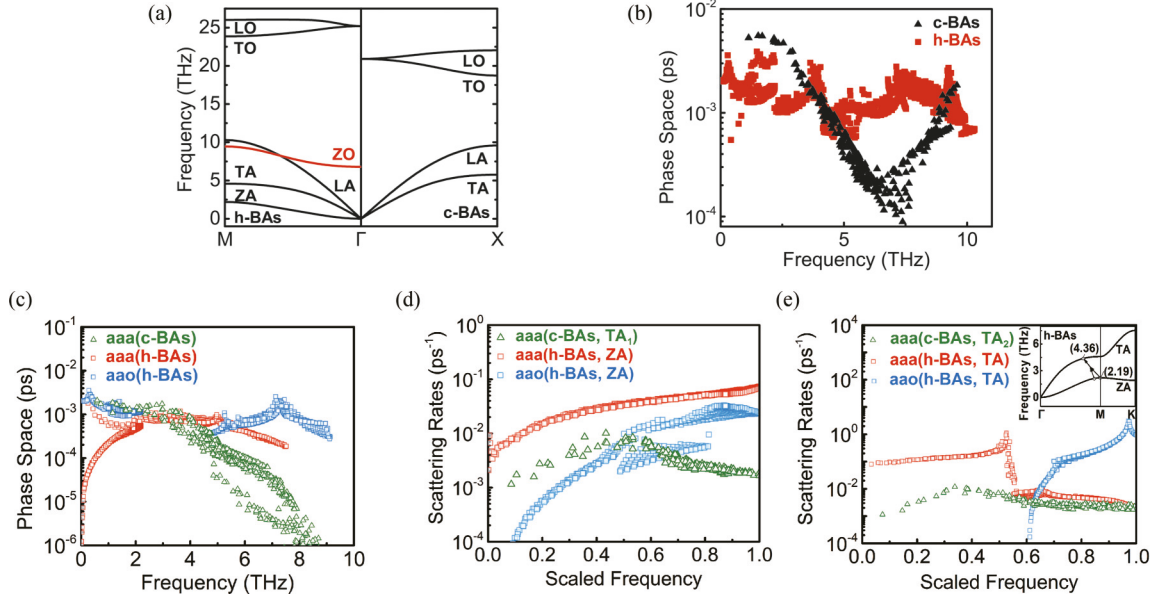


FIG. 6. Comparison of the dispersions and phonon transport properties of h-BAs and c-BAs. (a) Calculated phonon dispersions. (b) Total calculated scattering phase space versus phonon frequency. (c) Scattering phase space versus phonon frequency for different process types. (d) Calculated phonon scattering rates at room temperature versus scaled frequency for the lowest-frequency branches in h-BAs (ZA) and c-BAs (TA₁). (e) The same as (d) but for the second-lowest-frequency branches in h-BAs (TA) and c-BAs (TA₂). The figures show the scattering rates determined by different three-phonon processes: acoustic-acoustic-acoustic (aaa), acoustic-acoustic-optic (aoa), and acoustic-optic-optic (for aoo, see Fig. 14). The scattering rates are scaled by the highest frequency of each polarization for easier comparison. The inset of (d) illustrates a ZA + ZA → TA scattering process, which results in the kink observed in the scattering rates for the TA branch.

satisfy. To quantitatively analyze the thermal conductivity reduction due to the ZO phonon modes we artificially removed the scattering processes involving these and found that the κ_L contributed by TA and LA phonons increases 4~5 times but only increases by 20% for ZA phonons. With ZO phonon scattering, the isotopically pure κ_L is 457 W/m K, and the contributions from ZA, TA, and LA are 175.7, 127.7, and 109.5 W/m K, respectively. After removing the scattering processes involving ZO modes, κ_L increases to 1470 W/m K, and the contribution from ZA, TA, and LA phonons are 214, 581, and 527 W/m K, respectively. ZO modes significantly suppress the κ_L of TA and LA branches. To make further evaluation, we calculated the mode-dependent phonon-scattering phase space [Fig. 6(b)]. It shows that the scattering phase space of h-BAs is significantly larger than that of c-BAs in particular for the 4~6-THz phonon frequency range that makes a significant contribution to thermal transport in c-BAs.

Another possible explanation for lower κ_L in h-BAs compared to bulk c-BAs is the acoustic branches are much more separated in the former due to the quadratic behavior of the ZA branch at low frequency in h-BAs. Therefore, the 2D acoustic phonon band structure introduces more all-acoustic scattering channels in h-BAs compared with that in c-BAs. To quantify the acoustic bunching, we computed and compared the acoustic-acoustic-acoustic (aaa) and acoustic-acoustic-optical (aoa) scattering phase space of c-BAs and h-BAs in Fig. 6(c). It is found that acoustic bunching does not necessarily decrease the scattering phase space. At high frequency, the acoustic bunching in c-BAs makes its scattering phase space smaller than h-BAs. However, at low frequency, due to the quadratic feature in phonon dispersion, the acoustic bunching

becomes weaker, but the aaa scattering phase space for ZA branch is also smaller.

To further quantify the differences in anharmonic scattering between h-BAs and c-BAs, we calculated the branch-dependent phonon scattering rates for these materials for particular interacting channels: aaa, aao, acoustic-optical-optical (aoo), and optical-optical-optical (ooo). In particular, some of the scattering rates of the lowest-frequency (h-BAs-ZA; c-BAs-TA₁) and second-lowest-frequency (h-BAs-TA; c-BAs-TA₂) branches are compared in Figs. 6(d) and 6(e) and Fig. 14. The aao scattering rates for c-BAs are very weak due to its large phonon band gap, and thus are not shown. However, for h-BAs, aao scattering rates are non-negligible although much weaker than aaa scattering. This indicates stronger acoustic-optical interactions in h-BAs than in c-BAs, except at low frequencies where aoo scattering becomes important [49]. We note that aoo interactions involving a ZA phonon and two ZO phonons are forbidden by symmetry in the h-BX monolayers. To summarize, these calculations suggest that h-BAs has higher scattering rates and lower κ_L than c-BAs partly due to increased interactions between acoustic and ZO phonons for all phonon polarizations.

An interesting kink occurs in the TA scattering rates involving aaa processes for h-BAs around 4.3 THz [Fig. 6(e)]. The frequency for which this kink occurs is exactly twice the maximum frequency of the ZA branch. This result can be explained in terms of energy conservation and the reflection symmetry selection rule discussed in Sec. III B. An important symmetry-allowed scattering channel for the TA modes involves their interaction with two lower-frequency ZA modes [inset, Fig. 6(e)]. For TA phonons below ~4.3 THz

such scatterings are also allowed by energy conservation. However, for TA phonons above ~ 4.3 THz, energy cannot be conserved as this is two times the maximum energy of the ZA branch. Therefore, the suppressed scattering channels lead to a significant drop of scattering rates as shown by the kink in Fig. 6(e).

Higher-order anharmonicity is expected to be important for thermal transport at high temperatures or in strongly anharmonic materials. However, in both c-BAs [5] and graphene [64], four-phonon anharmonic scattering has been shown to give significant thermal resistance, even at room temperature, due to relatively weak three-phonon scattering in each system. Three-phonon scattering alone gives calculated RT κ_L of 2200 W/mK [4] and 3200 W/mK [65] in c-BAs and graphene, respectively, which reduce by 35% [5] and 75% (using an empirical potential) [64] when including four-phonon interactions. The monolayer h-BX materials considered here have significantly lower κ_L values than both c-BAs and graphene, suggesting that four-phonon scattering is not as important in determining their thermal transport properties. Unfortunately, the computational cost is too large to test this here. In addition, phonon frequency renormalization can be introduced by higher-order anharmonicity and the failure of the quasiharmonic approximation has been observed, even at room temperature and below, in tin selenide [66], but strong phonon renormalization is expected in strongly anharmonic materials with low thermal conductivities.

D. Comparison of phonon transport between h-BAs and graphene

In the previous section, increased acoustic-optical phonon scattering in h-BAs due to a midfrequency ZO branch was suggested as one of the causes of lower κ_L in h-BAs than that in c-BAs. However, graphene has an ultrahigh thermal conductivity despite also having a midfrequency ZO branch that provides scattering channels of the heat-carrying acoustic phonons. Here we compare the microscopic vibrational properties of monolayer h-BAs and graphene to further understand 2D transport.

The phonon dispersions of h-BAs and graphene are compared in Fig. 7(a) demonstrating two major differences: (1) h-BAs has a large phonon band gap that is absent in graphene, and (2) the graphene dispersion has a much larger overall frequency scale than that of h-BAs. Graphene's comparatively

small m_{avg} and strong covalent bonding (large θ_D) drive this overall frequency-scale difference and give sound velocities more than two times greater in graphene than in h-BAs [Fig. 7(b)]. As shown in Fig. 7(c), the phase space P_3 of graphene is much smaller than that of h-BAs, which indicates fewer scattering channels in graphene and reduced scattering rates. As discussed in Sec. III A, P_3 tends to scale inversely with the frequency scale of the overall dispersion. In addition, despite lacking a phonon band gap between the LO and TO branches and the acoustic spectrum, these optic branches have such high frequency that energy conservation forbids aao interactions for ZA and LO/TO modes. In other words, the large frequency scale mimics a phonon band gap for the ZA modes, which were shown to carry $\sim 75\%$ of the heat in graphene for certain cases [11]. Note that aao scattering among ZA and ZO modes is also forbidden by mirror reflection symmetry. The scattering phase space of h-BAs and graphene are given in Fig. 7(c), which demonstrates significantly more scattering channels in h-BAs and results in higher scattering rates.

E. Mean-free path spectra and size-dependent thermal conductivity

Rational ways to control thermal properties via size effects are of high scientific and technological interest, e.g., using nanostructuring for improved thermoelectrics or designing transport at multiple length scales for thermal management in electronic devices. In particular, phonon mean-free path (MFP) spectra have been intensively studied to understand the spectral contributions of the thermal conductivity over characteristic length scales of the heat carriers. *Ab initio* transport calculations have been directly tested by sophisticated measurements enabled by recently developed laser-based thermal spectroscopies [6,7,67]. Here, we calculated the MFP spectra in the h-BX monolayers and investigated the effects of finite sample width on their κ_L . MFPs describe the characteristic lengths that phonons travel, on average, before scattering. In general, MFPs are mode-dependent and can span across several orders of magnitude, from ~ 1 nm to ~ 1 mm. These spectral features are quantified by calculating the contributions to the overall thermal conductivity from phonons with MFPs smaller than a reference length Λ' [67,68].

$$\kappa^{\alpha\beta}(\Lambda') = \frac{1}{\Omega N} \sum_{\lambda} C_{\lambda} v_{\lambda}^{\alpha} v_{\lambda}^{\beta} \tau_{\lambda} \Theta(\Lambda' - |\mathbf{v}_{\lambda}| \tau_{\lambda}), \quad (11)$$

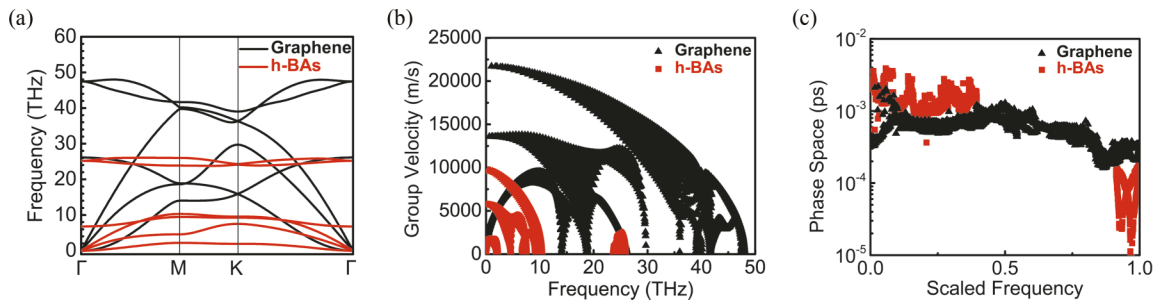


FIG. 7. Comparison of vibrational properties of monolayer h-BAs and graphene. Calculated (a) phonon dispersions, (b) group velocities, and (c) scattering phase spaces for h-BAs (red) and graphene (black). In (c) the frequencies are scaled by the highest phonon frequency for easier comparison.

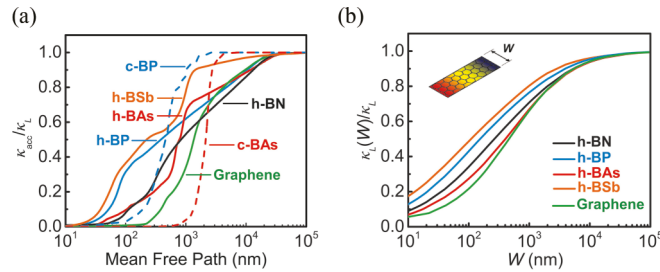


FIG. 8. Phonon mean-free path spectra and size-dependent thermal conductivity of h-BX monolayers. (a) Cumulated thermal conductivity [κ_{acc} ; Eq. (11)] versus phonon mean-free path (Λ) of h-BX monolayers compared with c-BP, c-BAs, and graphene. (b) Size-dependent thermal conductivity [$\kappa_L(W)$]. A nanoribbon geometry is used with diffuse scattering considered from edges of finite width W . Thermal conductivities in both figures are calculated for room temperature and are normalized by their corresponding bulk values (κ_L).

where Θ is the Heaviside function, C_λ is the mode-specific heat, and the other terms have been defined above. Figure 8(a) gives the calculated MFP spectra of the h-BX monolayers, as well as c-BAs, c-BP, and graphene. A large portion of the phonons in the h-BX monolayers have MFPs over $1 \mu\text{m}$ that contribute $\sim 50\%$ of the total κ_L at RT. Also, the heat carriers of h-BX monolayers have MFPs distributed over a wide range, while the heat carriers in c-BAs and c-BP all have MFP values within one order of magnitude. In comparison, the MFP spectra of the h-BX monolayers have different behaviors from c-BXs. Take h-BAs for example: After a rapid increase below $1.3 \mu\text{m}$, the accumulated h-BAs thermal conductivity begins a steady climb towards the peak. This feature arises from a large number of ZA phonons with long MFPs contributing to transport [see Fig. 16(a)]. For MFPs $> 1.3 \mu\text{m}$, only ZA modes contribute to the thermal conductivity. This behavior is not seen in the bulk cubic materials such as c-BAs and c-BP. Such MFP spectra are directly related to size-dependent κ_L and can provide important guidance for multiscale thermal transport.

To further evaluate size-dependent thermal transport in the h-BX monolayers, we included boundary scattering from finite nanoribbon width, but with infinite length along the transport direction [see Fig. 8(b)], by modifying a model [69] used in ShengBTE [18]. Specifically, the heat flux is applied along the nanoribbon and the deviation function \mathbf{F}_λ [see Eq. (2)] is a function of the spatial position across the width in the solution of the BTE. Here, the boundary is treated as totally diffusive, so $\mathbf{F}_\lambda = 0$ at the boundary and is described with exponentially decaying behavior from the center [69]. The cross-section averaged \mathbf{F}_λ can be derived within the iteration framework, from which the effective lattice thermal conductivity of the nanoribbon is obtained [70]. Figure 8(b) gives the width-dependent thermal conductivity $\kappa_L(W)$ of h-BX monolayers and graphene nanoribbons normalized by their bulk values. Finite sample width strongly affects the thermal conductivity for widths on the order of a micron. For example, for $W = 0.4 \mu\text{m}$, $\kappa_L(W)$ is reduced to 50, 56, 63, and 69% of their bulk values for h-BAs, h-BN, h-BP, and h-BSb, respectively. This analysis also indicates that finite-size effects

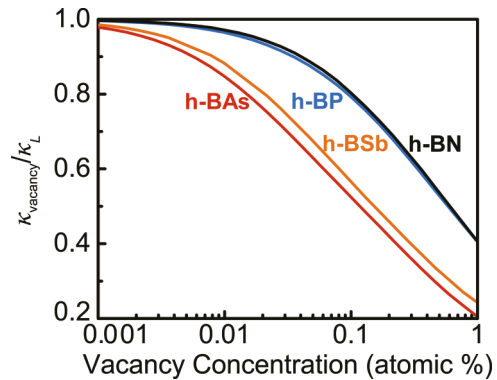


FIG. 9. Defect scattering effects. (a) Normalized thermal conductivity $\kappa_{vacancy}$ as a function of vacancy concentration from 0.001 to 1 (atomic %) at room temperature for h-BX monolayers. The vacancies are treated as mass defects similar to isotopes with zero mass.

should be more easily observed in h-BAs at considerably larger lengths than for the other materials.

F. Defect scattering and isotope effects

Defects inevitably exist in materials of practical interest and can often play a critical role in determining thermal transport. As discussed in Sec. II C, imperfections such as vacancies and other point defects can introduce additional phonon scattering which suppresses κ_L from its intrinsic value. To evaluate the effects of defects on thermal transport in h-BX monolayers, we considered phonon-defect scattering from mass variance due to vacancy defects on the X site (arsenic, nitrogen, phosphorus, and antimony). Note that defect-induced force constant changes are not considered here. κ_L of the h-BX monolayers are given in Fig. 9 as a function of vacancy concentration ranging from 0.001 to 1%. A stronger effect is seen for κ_L of h-BAs and h-BSb than for h-BN and h-BP, partly because vacancies induce a larger perturbation to the heavier As and Sb atoms. Isotopes can also play an important role in limiting thermal conductivity, although giving a smaller mass perturbation than vacancies. Arsenic is naturally isotopically pure, while Sb has an even mix of ^{121}Sb (57.21%) and ^{123}Sb (42.79%). Therefore, phonon-isotope scattering in h-BSb provides significant thermal resistance, 24% decrease of κ_L , even before considering phonon-vacancy scattering.

IV. SUMMARY AND CONCLUSIONS

From *ab initio* phonon Boltzmann transport calculations we investigated the lattice thermal conductivities of hexagonal single-layer h-BX compounds: boron nitride, boron phosphide, boron arsenide, and boron antimonide. Large κ_L was observed for these single-layer h-BX materials making them promising building blocks for thermal management applications. Microscopic physical insights were developed in comparing h-BX monolayer κ_L values with those of their bulk counterpart materials (c-BAs and c-BP), as well as prototypical 2D materials (graphene, silicene, and germanene). In particular, large κ_L , dimensionality-induced transport differences, and the possibility of hydrodynamic behaviors were

discussed in terms of features of the phonon dispersions: a-o gap, acoustic bunching, ZA phonon heat carriers, and midfrequency ZO phonon scattering. Strong normal scattering plays a key role in thermal transport for 2D h-BX materials, especially for ZA phonons. Furthermore, reflection symmetry of the 2D flat plane of h-BX materials restricts phonon-phonon scattering, thus leading to larger κ_L values than buckled 2D materials. For h-BAs, the midfrequency ZO branch and decreased acoustic bunching due to quadratic dispersion introduce extra thermal resistance compared with c-BAs. Phonon MFPs and size-dependent κ_L of the h-BX monolayers were calculated to understand length-scale effects on thermal transport, which are important for future device design. The effects of phonon-point-defect interactions were also estimated by calculating κ_L with vacancy defects in a mass-disorder model. This *ab initio* κ_L study gives predictions of the thermal properties of 2D boron-based compounds for thermal management applications and provides fundamental microscopic insights into phonon transport physics.

ACKNOWLEDGMENTS

Y.H. acknowledges support from a CAREER Award from the National Science Foundation (NSF) under Grant No. DMR-1753393, a Young Investigator Award from the United States Air Force Office of Scientific Research under Grant No. FA9550-17-1-0149, and an Alfred P. Sloan Research Fellowship under Grant No. FG-2019-11788. L.L. acknowledges support from the U. S. Department of Energy, Office of Science, Basic Energy Sciences, Materials Sciences and Engineering Division for contributions to calculation validation, and idea and manuscript development. This work used computational and storage services associated with the Hoffman 2 Shared Cluster provided by UCLA Institute for Digital Research and Education's Research Technology Group, and the Extreme Science and Engineering Discovery Environment (XSEDE), which is supported by NSF Grant No. ACI-1548562. Specifically, it used the Bridges system, which is supported by NSF Award No. ACI-1445606, at the Pittsburgh Supercomputing Center (PSC).

H.F. and H.W. contributed equally to this work.

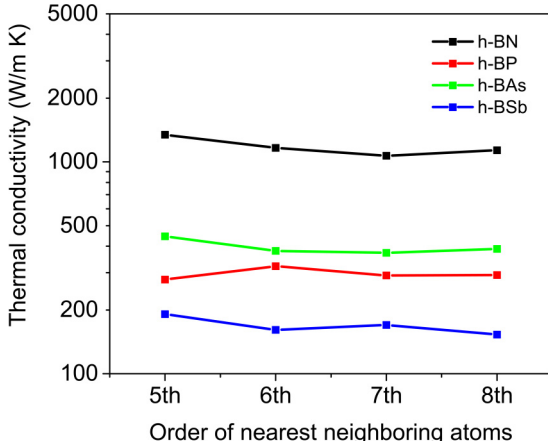


FIG. 10. Convergence test of thermal conductivity versus the cutoff radius for third-order IFCs.

TABLE II. Calculated thermal conductivity κ_L vs supercell size.

Supercell	h-BN	h-BP	h-BAs	h-BSb
72 atoms	1045	323	399	121
128 atoms	1134	292	388	153

APPENDIX A: CONVERGENCE TESTS OF THE LATTICE THERMAL CONDUCTIVITY

We have performed convergence tests of thermal conductivity versus the cutoff radius for third-order IFCs, supercell size, and mesh size, as well as sensitivity tests on the scalebroad settings. The convergence of thermal conductivity is tested with different cutoff radii (from fifth to eighth-nearest-neighboring atoms) for third-order IFCs on 128-atom supercells, as shown in Fig. 10. Results are converged within 10% when the cutoff radius reaches eighth-nearest-neighboring atoms. Thermal conductivities are calculated using IFCs from 72- and 128-atom supercells, shown in Table II. Figure 11 shows calculated thermal conductivities with five different ShengBTE [18] scalebroad settings: 0.9, 1.0, 1.05, 1.1, and 1.2. Results are converged when the scalebroad setting is above 1.1. In this work, thermal conductivity is obtained by using 1.1 as a scalebroad setting and fitting points to a curve of the form $\kappa_L = \kappa_L|_{N_1 \rightarrow \infty} [1 - e^{-N_1/A}]$, where $\kappa_L|_{N_1}$ is the thermal conductivity under mesh size $N_1 \times N_1 \times 1$, and A is a fitting parameter.

APPENDIX B: INTRINSIC PHONON SCATTERING RATES

We have performed the calculation of mode-dependent intrinsic phonon scattering rates for different h-BX materials. Contour plots of the calculated phonon-scattering rates for each phonon branch are compared and shown in Fig. 12.

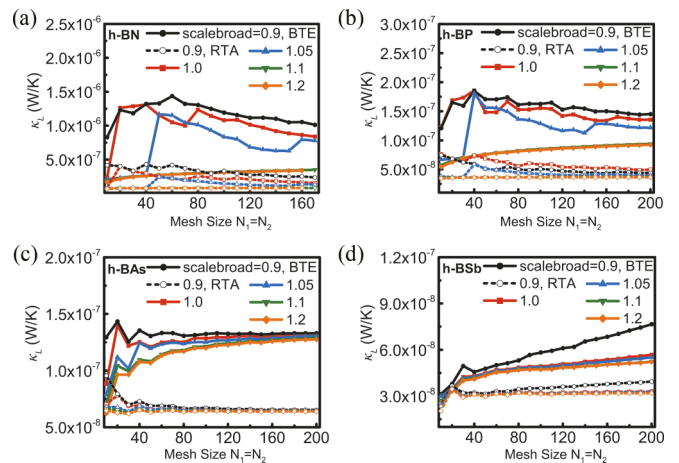


FIG. 11. Calculated lattice thermal conductivity κ_L in 2D units with respect to q -point grid density N for (a) h-BN, (b) h-BP, (c) h-BAs, and (d) h-BSb at room temperature for different scalebroad values.

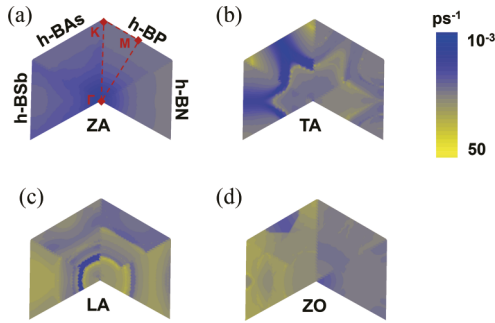


FIG. 12. Intrinsic scattering rates. Contour plot of the calculated phonon-scattering rates at room temperature for each phonon branch in h-BX monolayers (a) ZA, (b) TA, (c) LA, and (d) ZO in the irreducible segment of the Brillouin zone.

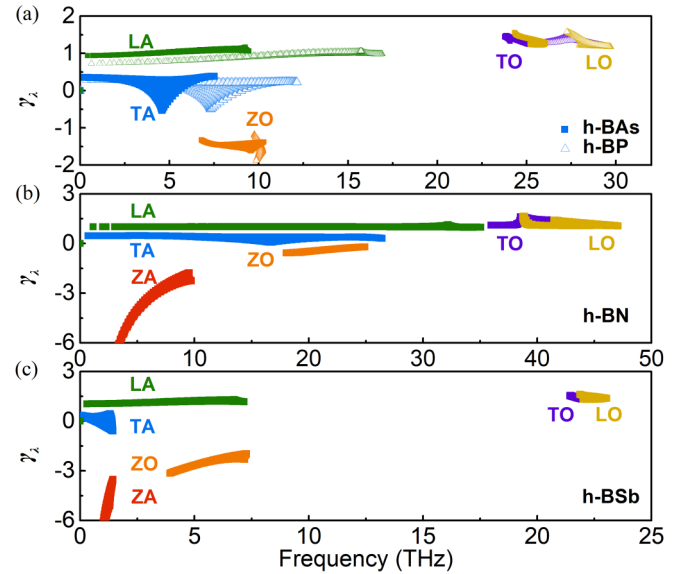


FIG. 13. Mode-dependent Grüneisen parameters (γ_λ) for (a) h-BAs (solid squares) compared with h-BP (hollow triangles), (b) h-BN, and (c) h-BSb. Colors are used to differentiate polarizations: ZA (red), TA (blue), LA (green), ZO (orange), TO (purple), and LO (yellow). The ZA Grüneisen parameters for h-BAs and h-BP are given in Fig. 4.

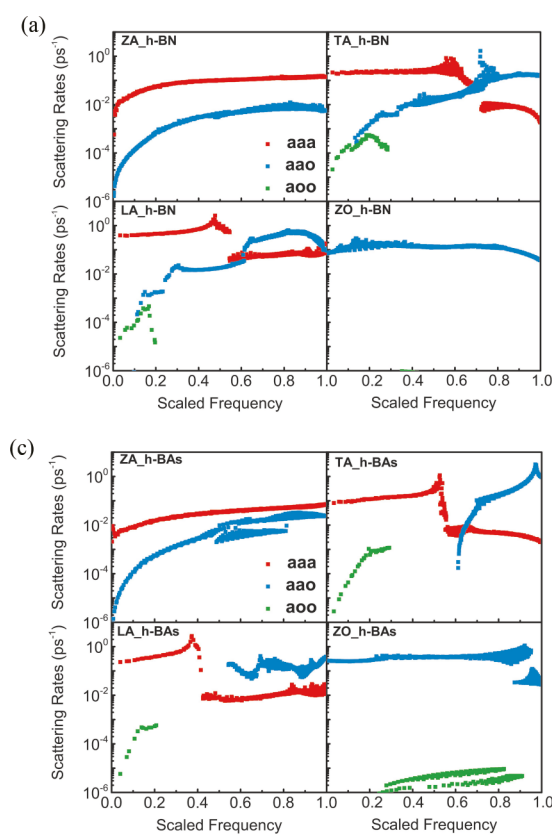


FIG. 14. Calculated scattering rates for hexagonal monolayer h-BX materials for the various types of processes: aaa (solid blue squares), aao (solid red squares), and aoo (solid green squares). The phonon frequencies are scaled by the highest frequency for each phonon branch. The aaa scattering in h-BAs increases monotonically with increasing frequency, while for bulk c-BAs these decrease in the middle to high-frequency range.

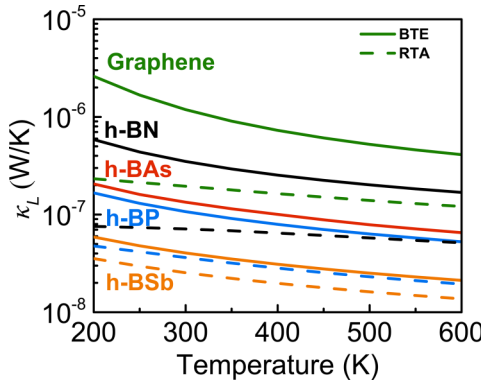


FIG. 15. Calculated lattice thermal conductivity κ_L in 2D units as a function of temperature for monolayer graphene (green), h-BN (black), h-BAs (red), and h-BSb (orange) with natural isotopic abundances. Solid curves correspond to full BTE solutions, while dashed curves correspond to RTA values.

APPENDIX D: IDENTIFICATION OF PHONON POLARIZATIONS AND SCATTERING TYPES

In Fig. 14, we distinguish the three-phonon processes into different types: acoustic-acoustic-acoustic (aaa), acoustic-acoustic-optical (aoa), and acoustic-optical-optical (aoo). We developed the following method to determine the phonon polarizations. To identify the polarization for each phonon mode, we started by labeling the polarizations for phonons with small q points near the Γ point, i.e., before any branch crossing takes place. For these small q points, the phonon modes follow the standard sequence of ZA, TA, LA, ZO, TO, and LO with increasing frequency. Then, we traced down each phonon branch to check the energy scale to determine if any two branches cross each other. In addition, to carefully verify the branch crossing, we zoomed in using a large q -mesh density along all high-symmetry directions. If crossing takes place, the phonon polarizations are reversely labeled between the corresponding two branches. For example, we have identified that for h-BAs, the ZO crosses the LA branch.

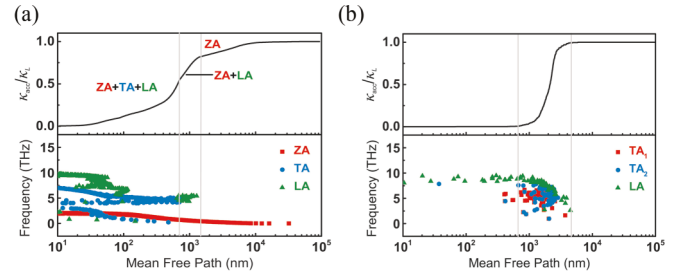


FIG. 16. Calculated phonon mean-free path distribution at room temperature for (a) h-BAs and (b) c-BAs. The top panels give the accumulated thermal conductivity normalized to their bulk values. The bottom panels give the mode-dependent mean-free paths correlated with their frequencies.

However, for h-BN, we identified that there is no crossing between the LO and TO branches, despite these two branches seeming to cross each other in the low-resolution Fig. 2(a).

APPENDIX E: COMPARISON BETWEEN RTA AND FULL BTE SOLUTIONS

We have performed the calculation of the thermal conductivity using both RTA and full BTE solutions. The results for different h-BXs materials are compared and plotted in Fig. 15. The calculated thermal conductivity of h-BXs from RTA is not as accurate and in general lower than that from full BTE solution, due to the strong normal scattering. More discussions can be found in Sec. III B.

APPENDIX F: PHONON MEAN FREE PATH SPECTRA AND MODE CONTRIBUTIONS BETWEEN h-BAs AND c-BAs

We have performed the calculation of the phonon mean free path spectra and the mode-dependent contribution to total lattice thermal conductivity. The results for h-BAs and c-BAs are plotted in Fig. 16 for comparison. More discussions can be found in Sec. III E.

[1] L. Lindsay, C. Hua, X. L. Ruan, and S. Lee, *Mater. Today Phys.* **7**, 106 (2018).

[2] N. Mingo, D. A. Stewart, D. A. Broido, L. Lindsay, and W. Li, in *Length-Scale Dependent Phonon Interactions*, edited by S. L. Shindé and G. P. Srivastava (Springer, New York, 2014), pp. 137–173.

[3] A. J. H. McGaughey, A. Jain, H. Y. Kim, and B. Fu, *J. Appl. Phys.* **125**, 011101 (2019).

[4] L. Lindsay, D. A. Broido, and T. L. Reinecke, *Phys. Rev. Lett.* **111**, 025901 (2013).

[5] T. Feng, L. Lindsay, and X. Ruan, *Phys. Rev. B* **96**, 161201(R) (2017).

[6] J. S. Kang, H. Wu, and Y. Hu, *Nano Lett.* **17**, 7507 (2017).

[7] J. S. Kang, M. Li, H. Wu, H. Nguyen, and Y. Hu, *Science* **361**, 575 (2018).

[8] S. Li, Q. Zheng, Y. Lv, X. Liu, X. Wang, P. Y. Huang, D. G. Cahill, and B. Lv, *Science* **361**, 579 (2018).

[9] F. Tian, B. Song, X. Chen, N. K. Ravichandran, Y. Lv, K. Chen, S. Sullivan, J. Kim, Y. Zhou, T. H. Liu, M. Goni, Z. Ding, J. Sun, G. A. G. U. Gamage, H. Sun, H. Ziyae, S. Huyan, L. Deng, J. Zhou, A. J. Schmidt, S. Chen, C.-W. Chu, P. Y. Huang, D. Broido, L. Shi, G. Chen, and Z. Ren, *Science* **361**, 582 (2018).

[10] D. A. Broido, M. Malorny, G. Birner, N. Mingo, and D. A. Stewart, *Appl. Phys. Lett.* **91**, 231922 (2007).

[11] J. H. Seol, I. Jo, A. L. Moore, L. Lindsay, Z. H. Aitken, M. T. Pettes, X. Li, Z. Yao, R. Huang, D. Broido, N. Mingo, R. S. Ruoff, and L. Shi, *Science* **328**, 213 (2010).

[12] L. Lindsay, D. A. Broido, and N. Mingo, *Phys. Rev. B* **82**, 115427 (2010).

[13] R. Peierls, *Ann. Phys.* **395**, 1055 (1929).

[14] R. E. Peierls, *Quantum Theory of Solids* (Oxford University Press, London, 1955).

[15] M. Omini and A. Sparavigna, *Phys. Rev. B* **53**, 9064 (1996).

[16] D. A. Broido, A. Ward, and N. Mingo, *Phys. Rev. B* **72**, 014308 (2005).

[17] J. M. Ziman, *Principles of the Theory of Solids* (Cambridge University Press, Cambridge, 1972).

[18] W. Li, J. Carrete, N. A. Katcho, and N. Mingo, *Comput. Phys. Commun.* **185**, 1747 (2014).

[19] A. Ward, D. A. Broido, D. A. Stewart, and G. Deinzer, *Phys. Rev. B* **80**, 125203 (2009).

[20] K. Parlinski, Z. Q. Li, and Y. Kawazoe, *Phys. Rev. Lett.* **78**, 4063 (1997).

[21] L. Chaput, A. Togo, I. Tanaka, and G. Hug, *Phys. Rev. B* **84**, 094302 (2011).

[22] W. Li, L. Lindsay, D. A. Broido, D. A. Stewart, and N. Mingo, *Phys. Rev. B* **86**, 174307 (2012).

[23] L. Lindsay, D. A. Broido, and N. Mingo, *Phys. Rev. B* **83**, 235428 (2011).

[24] L. Lindsay, D. A. Broido, and T. L. Reinecke, *Phys. Rev. B* **87**, 165201 (2013).

[25] D. C. Gazis and R. F. Wallis, *Phys. Rev.* **151**, 578 (1966).

[26] S. F. Wang, H. L. Zhang, and X. Z. Wu, *J. Phys.: Condens. Matter* **19**, 386233 (2007).

[27] N. Bonini, J. Garg, and N. Marzari, *Nano Lett.* **12**, 2673 (2012).

[28] M. Born and K. Huang, *Dynamical Theory of Crystal Lattices* (Clarendon, Oxford, 1954).

[29] J. Carrete, W. Li, L. Lindsay, D. A. Broido, L. J. Gallego, and N. Mingo, *Mater. Res. Lett.* **4**, 204 (2016).

[30] C. Shi and X. Luo, arXiv:1811.05597.

[31] S.-i. Tamura, *Phys. Rev. B* **27**, 858 (1983).

[32] L. Lindsay, D. A. Broido, and T. L. Reinecke, *Phys. Rev. B* **88**, 144306 (2013).

[33] N. A. Katcho, J. Carrete, W. Li, and N. Mingo, *Phys. Rev. B* **90**, 094117 (2014).

[34] N. H. Protik, J. Carrete, N. A. Katcho, N. Mingo, and D. Broido, *Phys. Rev. B* **94**, 045207 (2016).

[35] P. Giannozzi, S. Baroni, N. Bonini, M. Calandra, R. Car, C. Cavazzoni, D. Ceresoli, G. L. Chiarotti, M. Cococcioni, I. Dabo, A. D. Corso, S. de Gironcoli, S. Fabris, G. Fratesi, R. Gebauer, U. Gerstmann, C. Gougaud, A. Kokalj, M. Lazzeri, L. Martin-Samos, N. Marzari, F. Mauri, R. Mazzarello, S. Paolini, A. Pasquarello, L. Paulatto, C. Sbraccia, S. Scandolo, G. Sclauzero, A. P. Seitsonen, A. Smogunov, P. Umari, and R. M. Wentzcovitch, *J. Phys.: Condens. Matter* **21**, 395502 (2009).

[36] P. Giannozzi, O. Andreussi, T. Brumme, O. Bunau, M. B. Nardelli, M. Calandra, R. Car, C. Cavazzoni, D. Ceresoli, M. Cococcioni, N. Colonna, I. Carnimeo, A. D. Corso, S. de Gironcoli, P. Delugas, R. A. DiStasio, A. Ferretti, A. Floris, G. Fratesi, G. Fugallo, R. Gebauer, U. Gerstmann, F. Giustino, T. Gorni, J. Jia, M. Kawamura, H.-Y. Ko, A. Kokalj, E. Küçükbenli, M. Lazzeri, M. Marsili, N. Marzari, F. Mauri, N. L. Nguyen, H.-V. Nguyen, A. Otero-de-la-Roza, L. Paulatto, S. Poncet, D. Rocca, R. Sabatini, B. Santra, M. Schlipf, A. P. Seitsonen, A. Smogunov, I. Timrov, T. Thonhauser, P. Umari, N. Vast, X. Wu, and S. Baroni, *J. Phys.: Condens. Matter* **29**, 465901 (2017).

[37] D. R. Hamann, *Phys. Rev. B* **88**, 085117 (2013).

[38] We used the SG15 Optimized Norm-Conserving Vanderbilt (ONCV) pseudopotentials SG15.LDA. UPF generated using the code ONCVPSP (Optimized Norm-Conserving Vanderbilt PSeudopotential) scalar-relativistic version 2.1.1, March 26, 2014 by D. R. Hamann from: http://quantum-simulation.org/potentials/sg15_oncv/.

[39] J. Carrete, B. Vermeersch, A. Katre, A. van Roekeghem, T. Wang, G. K. H. Madsen, and N. Mingo, *Comput. Phys. Commun.* **220**, 351 (2017).

[40] We used the pseudopotentials B.pz-n-kjpaw_psl.0.1.UPF and P.pz-n-kjpaw_psl.0.1.UPF from the QUANTUM ESPRESSO pseudopotential data base: <http://www.quantum-espresso.org/pseudopotentials>.

[41] S. Baroni, S. de Gironcoli, A. Dal Corso, and P. Giannozzi, *Rev. Mod. Phys.* **73**, 515 (2001).

[42] B. Peng, D. Zhang, H. Zhang, H. Shao, G. Ni, Y. Zhu, and H. Zhu, *Nanoscale* **9**, 7397 (2017).

[43] X. Gu, Y. Wei, X. Yin, B. Li, and R. Yang, *Rev. Mod. Phys.* **90**, 041002 (2018).

[44] B. Peng, H. Zhang, H. Shao, Y. Xu, G. Ni, R. Zhang, and H. Zhu, *Phys. Rev. B* **94**, 245420 (2016).

[45] Y. D. Kuang, L. Lindsay, S. Q. Shi, and G. P. Zheng, *Nanoscale* **8**, 3760 (2016).

[46] G. A. Slack, *J. Phys. Chem. Solids* **34**, 321 (1973).

[47] L. Lindsay, D. A. Broido, and T. L. Reinecke, *Phys. Rev. Lett.* **109**, 095901 (2012).

[48] D. A. Broido, L. Lindsay, and T. L. Reinecke, *Phys. Rev. B* **88**, 214303 (2013).

[49] S. Mukhopadhyay, L. Lindsay, and D. S. Parker, *Phys. Rev. B* **93**, 224301 (2016).

[50] E. Pop, V. Varshney, and A. K. Roy, *MRS Bull.* **37**, 1273 (2012).

[51] A. A. Balandin, *Nat. Mater.* **10**, 569 (2011).

[52] S. Chen, Q. Wu, C. Mishra, J. Kang, H. Zhang, K. Cho, W. Cai, A. A. Balandin, and R. S. Ruoff, *Nat. Mater.* **11**, 203 (2012).

[53] L. Lindsay and D. A. Broido, *J. Phys.: Condens. Matter* **20**, 165209 (2008).

[54] J. Serrano, A. Bosak, R. Arenal, M. Krisch, K. Watanabe, T. Taniguchi, H. Kanda, A. Rubio, and L. Wirtz, *Phys. Rev. Lett.* **98**, 095503 (2007).

[55] A. N. Norris and D. A. Rebinsky, *J. Vibr. Acoust.* **116**, 457 (1994).

[56] G. D. Mahan and G. S. Jeon, *Phys. Rev. B* **70**, 075405 (2004).

[57] L. Lindsay, D. A. Broido, and N. Mingo, *Phys. Rev. B* **80**, 125407 (2009).

[58] E. Mariani and F. von Oppen, *Phys. Rev. Lett.* **100**, 076801 (2008).

[59] W. H. Press, S. A. Teukolsky, W. T. Vetterling, and B. P. Flannery, *Numerical Recipes in Fortran* (Cambridge University Press, Cambridge, UK, 1992).

[60] N. W. Ashcroft and N. D. Mermin, *Solid State Physics* (Holt, Rinehart and Winston, New York, 1976).

[61] L. Lindsay, *Nanoscale Microscale Thermophys. Eng.* **20**, 67 (2016).

[62] A. Cepellotti, G. Fugallo, L. Paulatto, M. Lazzeri, F. Mauri, and N. Marzari, *Nat. Commun.* **6**, 6400 (2015).

- [63] S. Lee, D. Broido, K. Esfarjani, and G. Chen, *Nat. Commun.* **6**, 6290 (2015).
- [64] T. Feng and X. Ruan, *Phys. Rev. B* **97**, 045202 (2018).
- [65] L. Lindsay, W. Li, J. Carrete, N. Mingo, D. A. Broido, and T. L. Reinecke, *Phys. Rev. B* **89**, 155426 (2014).
- [66] J. S. Kang, H. Wu, M. Li, and Y. Hu, *Nano Letters*, doi: 10.1021/acs.nanolett.9b01056.
- [67] Y. Hu, L. Zeng, A. J. Minnich, M. S. Dresselhaus, and G. Chen, *Nat. Nanotechnol.* **10**, 701 (2015).
- [68] F. Yang and C. Dames, *Phys. Rev. B* **87**, 035437 (2013).
- [69] R. G. Chambers, *Proc. R. Soc. London, Ser. A* **202**, 378 (1950).
- [70] W. Li, N. Mingo, L. Lindsay, D. A. Broido, D. A. Stewart, and N. A. Katcho, *Phys. Rev. B* **85**, 195436 (2012).